HHS Public Access

Author manuscript

Nat Methods. Author manuscript; available in PMC 2011 October 01.

Published in final edited form as:

Nat Methods. 2011 April ; 8(4): 327–333. doi:10.1038/nmeth.1571.

Confined Activation and Subdiffractive Localization Enables Whole-Cell PALM with Genetically Expressed Probes

Andrew G. York[1,*], **Alireza Ghitani**[1], **Alipasha Vaziri**[2,3], **Michael W. Davidson**[4], and **Hari Shroff**[1]

[1] Section on High Resolution Optical Imaging, National Institute of Biomedical Imaging and Bioengineering, National Institutes of Health, 13 South Drive, Bethesda, MD 20892

[2] Research Institute of Molecular Pathology (IMP), Dr. Bohr-Gasse 7, A-1030 Vienna, Austria

[3] Max F. Perutz Laboratories (MFPL), University of Vienna, Dr. Bohr-Gasse 9, A-1030 Vienna, Austria

[4] National High Magnetic Field Laboratory and Department of Biological Science, Florida State University, Tallahassee, FL 32310

Abstract

We demonstrate 3D superresolution microscopy in whole fixed cells using photoactivated localization microscopy (PALM). The use of the bright, genetically expressed fluorescent marker photoactivatable mCherry (PA-mCherry1) in combination with near diffraction-limited confinement of photoactivation using two-photon illumination and 3D localization methods allowed us to investigate a variety of cellular structures at <50 nm lateral and <100 nm axial resolution. Compared to existing methods, we substantially reduce excitation and bleaching of unlocalized markers, enabling 3D PALM imaging with high localization density in thick structures. Our 3D localization algorithms based on cross-correlation do not rely on idealized noise models or specific optical configurations, allowing flexible instrument design. Generation of appropriate fusion constructs and expression in Cos7 cells allowed us to image invaginations of the nuclear membrane, vimentin fibrils, the mitochondrial network, and the endoplasmic reticulum at depths greater than 8 μm.

The marriage of fluorescence microscopy with labeling technologies is an invaluable tool for cell biologists, providing three dimensional views of protein distributions with high contrast and specificity while minimizing sample perturbation. Despite these advantages, the diffraction limit historically placed a lower bound of ~250 nm on the smallest structures that may be resolved with optical wavelengths. X-ray microscopy[1] and electron microscopy[2]

[*]Correspondence should be addressed to A.Y. (andrew.g.york+naturemethods@gmail.com).

Author contributions

A.G.Y., A.G., and H.S. conceived, designed, and built the experimental setup. A.G.Y. wrote the analysis code. A.G. and H.S. took the data. A.G.Y., A.G., and H.S. analyzed the data. M.W.D. and A.V. contributed reagents and materials. A.G.Y., M.W.D. and H.S. wrote the paper. All authors edited and refined the paper.

provide higher spatial resolution, but usually sacrifice contrast and involve more complex sample preparation.

A number of optical superresolution techniques now allow spatial resolutions down to ~20 nm while retaining the advantages of fluorescence microscopy. Structured illumination microscopy[3] allows a two-fold increase in 3D resolution over the diffraction limit[4], while 3D stimulated emission depletion microscopy[5] has been demonstrated with an isotropic resolution of ~40 nm[6]. A different class of 'pointillist' techniques ((f)PALM[7,8], STORM[9]) rely on repeated stochastic photoactivation of single molecules and their subsequent localization over thousands of widefield images to provide 20–30 nm resolution in 2D[7] and sub-100 nm resolution in 3D[10]. Higher resolution may be achieved by combining interferometry with pointillist methods[11], but this approach places severe constraints on sample geometry and is limited to a depth within ~500 nm of the coverslip.

As pointillist methods build superresolution images literally molecule-by-molecule, maximizing the number of successful localizations is critical for resolving small structures. This procedure depends on isolating the fluorescent signal emitted from a single activated molecule from the potentially much larger sea of background arising from cellular autofluorescence and extraneous activation and excitation of other molecules. For surface bound systems or thin samples (< 200 nm), total internal reflection[12] may be used to limit background, allowing even relatively dim, genetically expressed photoactivatable fluorescent proteins (PA-FPs) to be utilized. These markers are especially useful in superresolution imaging, offering greater specificity and effectively higher labeling densities than brighter, exogenously introduced dyes.

Imaging thicker, three-dimensional samples is problematic, as widefield illumination (Fig. 1a) activates and excites out-of-focus probe molecules, increasing background and generally precluding the use of dim PA-FPs. Furthermore, if an out-of-focus molecule is not localized, it is wasted, decreasing the effective label density and reducing image resolution.

One strategy that alleviates background and is compatible with PA-FPs relies on two-photon illumination for confinement of activation to the vicinity of the focal plane (Fig. 1b) and subsequent 2D subdiffractive molecular localization under widefield excitation[13,14]. As activation is confined to ~+/−1μm of focus, these methods make better use of the available molecular budget than widefield illumination. However, 2D localization algorithms utilize only those molecules within ~ 100nm of focus, wasting the remainder and leaving axial 'gaps' in the reconstructed 3D PALM volume.

An alternate strategy for 3D pointillist superresolution combines widefield illumination of bright, exogenously introduced dyes with 3D subdiffractive localization techniques[15] for ~20–30 nm lateral and ~50–60 nm axial localization precision at depths up to 3 μm[16]. By localizing molecules within ~+/−300 nm of the focal plane, these techniques better fill the imaging volume, although still wasting localizations and increasing background as the entire cell is illuminated simultaneously. The fraction of 'wasted' localizations worsens for thicker samples. This is especially problematic for fluorescent tags that bleach rapidly, like many PA-FPs

We combined and improved these two strategies to enable whole-cell PALM imaging at <100 nm axial and <50 nm lateral resolution with the genetically expressed fluorescent marker photoactivatable mCherry (PA-mCherry1[17]), at depths > 8 μm. First, we reduced out-of-focus background by using rapid, line-scanning temporal focusing to confine photoactivation to ~+/−600 nm of the focal plane (Fig. 1c). Second, we developed a 3D localization algorithm that works over this full axial range, does not rely on idealized models of optics or noise sources, and is more tolerant of microscope aberrations (Fig. 1d). Compared to existing methods for 3D PALM or STORM, these improvements eliminate axial gaps[13,14], mitigate background, and reduce wasted probe molecules for improved localization density, enabling superresolution at greater imaging depths than previously realized. We demonstrated the utility of this technique by investigating a variety of 3D cellular structures including mitochondria, the endoplasmic reticulum, vimentin filaments, and nuclei.

Results

PALM and STORM typically employ widefield activation and excitation for sample illumination (Fig. 1a). While easy to implement on epi-fluorescence microscopes, widefield illumination activates and excites molecules outside the focal volume, causing an increased fluorescent background and unnecessary photobleaching. Methods that confine illumination to the focal plane (Fig. 1b), such as two-photon microscopy (2PM[18]), alleviate these problems.

Confined photoactivation for reduced background

Conventional temporal focusing[19] microscopy[20] confines two-photon illumination to a single plane by scanning an intense line focus across the sample on a picosecond timescale, enabling optical sectioning at depths > 100 μm[13]. We previously showed that this technique can confine the photoactivation of the PA-FP Dronpa[21], allowing superresolution imaging in cells at depths up to 5 μm, with ~50 nm lateral localization precision[13]. Despite the potential usefulness of the technique, we identified three areas for significant methodological improvement. First, the best optical sectioning provided by conventional temporal focusing is limited to ~2 μm, ~2x worse than the sectioning of point-scanning two-photon methods. Second, Dronpa is a non-ideal PALM probe with low emitted signal per localization and relatively poor contrast ratio (ratio of fluorescence intensity between activated and nonactivated states). Finally, no attempt was made to combine the technique with axial localization for superresolution in z.

We improved optical sectioning while maintaining high frame rates by implementing temporal focusing in line-scanning mode[22] (Fig. 1c and Supplementary Fig. 1). Line-scanning temporal focusing offers the sectioning quality of point-scanning 2PM (Supplementary Fig. 2) but the increased scan speed of line-scanning 2PM by combining spatial focusing and temporal focusing in orthogonal directions. The temporal focus scans an intense point left to right on a picosecond time scale, illuminating a line, and a galvanometric mirror scans the illuminated line up-down on a millisecond timescale to cover the full imaging field (Supplementary Fig. 3). Acquisition times for conventional point-

scanning 2PM are considerably longer (~0.1 – 1 s for the same field of view, a poor match for PALM-imaging at high frame rates), although resonant scanning systems are faster (~20 ms at the cost of additional instrument complexity) and could be adapted for confined activation. Optimizing line-scanning temporal focusing allowed us to achieve superior axial sectioning with reduced out-of-focus haze and FWHM (< 1.2 μm) compared to conventional temporal focusing and widefield illumination (Fig. 1c, **Methods**, and Supplementary Note 1).

Dronpa has been used in single-[13] and dual-color PALM[23], but emits less fluorescence and possesses a lower contrast ratio than many PA-FPs, so we searched for alternate PA-FPs that are two photon activatable (2PA). PA-mCherry1[17] is reportedly much better suited to PALM, with moderate brightness and high contrast ratio. Upon exposure to 800 nm activation light, we observed complete photoconversion of purified PA-mCherry1 proteins on a surface, and improved axial activation confinement under scanning temporal focus compared to conventional temporal focus or 1PA (Supplementary Fig. 4), prompting us to use this probe for 3D PALM.

3D localization with an experimentally measured PSF

Performing PALM throughout an entire cellular volume with axial resolution significantly below the diffraction limit (~750 nm for our 1.2 NA water immersion objective lens) requires localization in the axial as well as lateral dimensions. Subdiffractive axial localization in the context of 3D whole cell imaging has been demonstrated using exogenously introduced synthetic dyes[10],[16], but not with PA-FPs, presumably due to their lower fluorescence output. Although the nature of the method for subdiffractive localization varies (astigmatism[10], biplane imaging[24], or helical point spread functions (PSF)[25] have been used), an emission PSF that varies rapidly with axial position is common to all methods. After axial variation has been introduced, experimental data are fit to a theoretical model PSF using a least squares[10] or maximum likelihood estimator[26], which also requires a model of noise. Localization precision thus depends on how well these models describe experimental conditions, especially important when emitted fluorescence is dim, as in the case of PA-FPs. Previous methods used an experimentally measured PSF[15] for 3D superresolution in biplane PALM[24], but such approaches still rely on a model of noise and the measurement of quantities such as total signal photoelectrons and total background photoelectrons.

Experimental noise is difficult to model accurately, and background subtraction is complicated in thicker samples where out-of-focus fluorescence varies spatially and temporally during acquisition. Even under constant illumination, different pixels in our CCD chip have different noise and background levels[27]. Experimental PSFs are also difficult to model accurately. Introducing a cylindrical lens into our imaging system caused the PSF to resemble an ellipse whose minor and major dimensions varied as a function of z, but close inspection revealed features not easily accounted for by a 2D elliptical Gaussian function as has been previously used for astigmatic based localization[10] (Fig. 1d, a 2D elliptical Gaussian fit to the molecular image at z=−1 μm gives a localization error of hundreds of nm). Furthermore, although PSFs were translationally invariant (Supplementary Fig. 5), they

varied noticeably from experiment to experiment (Supplementary Fig. 6, presumably due to variations in coverslip thickness or tilt[28]). Rather than attempting to fit a molecular PSF to an *ad hoc* theoretical model function, we directly measured the 3D PSF of a subdiffractive, non-bleaching gold bead and performed a cross-correlation[29] between molecular and bead PSFs to obtain subdiffractive 3D molecular localization (**Methods** and Supplementary Note 2), bypassing the problems of a model that imperfectly described our PSF, background, and noise. Control experiments comparing the 100 nm gold bead PSF with a ~6 nm quantum dot PSF (closer to the size of PA-FP, Supplementary Fig. 7), and comparing images of the gold bead to molecular images at different axial positions (Supplementary Fig. 8) demonstrate the viability of our cross-correlation method.

Inherent aberrations of our microscope gave sufficient axial PSF variation to resolve axial steps of 50 nm using a 100 nm gold fiducial bead (Supplementary Fig. 9). Adding a cylindrical lens to the beam path improved signal-to-noise, spreading the signal from out-of-focus molecules over fewer pixels (while introducing a slight but correctable distortion, Supplementary Fig. 10) and allowed us to resolve the thickness of a layer of purified PA-mCherry1 protein molecules (dimmer than a typical fiducial marker) to < 150 nm (Supplementary Fig. 11). This measurement represents an upper bound on axial localization precision, as coverslip inhomogeneities, surface roughness and tilt broaden the measured thickness of the protein layer, but were not accounted for. Lateral localization precision is difficult to measure for single PA-mCherry1 molecules, but is ~20–40 nm for gold fiducial particles of similar brightness (Supplementary Fig. 12).

Our algorithm works with different imaging configurations (e.g. with or without a cylindrical lens) and is implemented in a free, platform-independent language[30] (see Supplementary Software and http://code.google.com/p/palm3d for details), allowing this localization method to be performed using any widefield microscope with a precise axial positioning stage. A 1.4 GHz laptop computer processed ~20–60 localizations per second per CPU, a total processing time of less than a day for the 3D datasets described below. Images are rendered as histograms (discussed in Supplementary Note 3 and Supplementary Figs. 13–14), with resolution determined by two factors: localization precision (how precisely the x, y, z coordinates of each molecule are determined) and localization density. Typically our resolution is more limited by localization density than localization precision.

Confined activation with 3D localization improves PALM

To demonstrate that the combination of line-scanning temporal focus with our model-independent subdiffractive 3D localization algorithm improves the number of captured localizations compared to previous widefield methods[10], we PALM-imaged different regions of a Cos7 cell transfected with PA-mCherry1 fused to the mitochondrial targeting signal of human cytochrome C oxidase subunit VIII with either confined or widefield illumination (Fig. 2), proceeding until all PA-mCherry1 molecules bleached. By appropriately blocking illumination in image planes conjugate to the sample plane, we restricted line-scanning temporal focus to the top portion of the field of view (above dashed yellow line), and widefield activation to the bottom portion (below dashed yellow line). Evident in both xy and zy views, confining activation to the vicinity of the focal plane with

line-scanning temporal focus increases the number of localizations > 2x over the ~3 μm thick sample, and shows mitochondria persisting deeper into the cell compared to widefield activation, as fewer molecules outside the imaging plane are photoactivated but not localized. Using widefield illumination, most localizations were near the coverslip (Fig. 2, zy view), likely because we started imaging there. We observed similar results in other cells, indicating that confining activation to the vicinity of the focal plane conserves the molecular budget, resulting in greater numbers of localizations compared to widefield activation. We note that the addition of our 3D subdiffractive localization algorithm substantially improves previous methods that relied on confined activation[13,14] and 2D subdiffractive localization (Supplementary Fig. 15).

3D whole cell PALM

Combining line-scanning temporal focusing for two-photon activation with 3D subdiffractive localization allowed us to 'fill the gaps' between 2D imaging planes when PALM-imaging whole fixed cells, and to better conserve the molecular budget available in the sample. We next demonstrated the applicability of the technique by imaging a variety of 3D structures in whole fixed cells (Figs. 3–6, Supplementary Fig. 16). A 3D PALM histogram of a Cos7 cell transfected with PA-mCherry1 fused to the mitochondrial targeting signal of human cytochrome C oxidase subunit VIII is presented in Figure 3 and Supplementary Video 1. The mitochondrial network spans an imaging field of ~30 × 30 μm over the ~3 μm depth of the cell (maximum intensity projections in Fig. 3a). 3D PALM resolved small features such as densely-labeled 'cores' within mitochondria (whose diameter ranged from < 100 nm to > 300 nm), surrounded by low-density halos (examples highlighted by white arrows in Figure 3a). A zoomed-in version of three such cores (Fig. 3b, detailed view of yellow boxes in Fig. 3a) shows top (xy) and front (xz) maximum-intensity projections of the core/halo structure, compared to diffraction-limited images (blurred to 250 nm lateral, 750 nm axial resolution). In diffraction-limited images, the core-halo structure is invisible, the axial extent of the cores is distorted, and the leftmost core is nearly obscured. Individual z-sections 75 nm thick (Figure 3c, detail of the blue boxes in Fig. 3a) reinforce these findings, with several voids (white arrowheads) visible only in the superresolved images.

As another example of 3D PALM, we PALM-imaged PA-mCherry1 with an N-terminal calreticulin signal peptide and C-terminal KDEL retention sequence, targeting the endoplasmic reticulum (ER) (Fig. 4 and Supplementary Video 2). In addition to the membranous honeycomb-like structures previously reported using diffraction limited fluorescence microscopy[31], we resolved a thin lining surrounding the nucleus (Fig 4b, detailed view of yellow box in Fig. 4a). The apparent thickness of this lining was ~25 nm in a 25 nm z section (arrow, Fig 4b), well beneath the diffraction limit and suggesting the ER fusion proteins also targeted at or close to the nuclear membrane. Higher magnification views of honeycomb ER structures are shown in Figure 4c,d (blue and white boxed regions in Fig. 4a). Although diffraction-limited imaging resolves large voids in lateral views (Fig. 4c, bottom left panel), internal structure evident in an xz slice is completely obscured (Fig. 4c, lower right panel). Fine structure in the higher magnification view in Fig. 4d is invisible at the diffraction limit, as demonstrated in the higher magnification xz views in Fig. 4e.

Three successive xz slices spaced 25 nm apart in the y direction show that small membrane-enclosed structures persist on smaller length scales, resolved axially to 50–75 nm.

Whole cell 3D PALM may also be applied to filamentous structures, as demonstrated by imaging vimentin-PA-mCherry1 fusions (Fig. 5 and Supplementary Video 3). As others have noted in living cells[32], we observed a distribution in the size and thickness of vimentin fibrils, with some fibrils appearing as thick as ~650 nm, and others close to our resolution limit (Fig 5a, inset). The filaments have a complex 3D structure, as shown in Fig 5b where color indicates axial position; the 3D structure is shown as two 1.5 μm thick slices to prevent overlapping filaments from obscuring one another. A thick filament extends over >2 μm axially (arrowheads in Fig. 5a,b), confirming that our drift correction method (discussed in **Methods**) successfully aligns images taken at a range of different axial positions.

We resolved subdiffractive nuclear structures at depths up to ~7 μm when imaging PA-mCherry1-lamin B1 fusions (Fig. 6 and Supplementary Video 4). Invaginations of the nuclear envelope are evident, as are void regions of excluded volume. Regions of the nuclear membrane are resolved to < 100 nm (white arrow in Fig. 6). Additional experiments demonstrated that our approach enables single molecule imaging at depths > 8 μm (Supplementary Video 5).

Discussion

We expect depth-dependent aberrations and scattering to limit our imaging depth, but have not explored this regime, as our cellular samples were < 10 μm thick. While the methods we developed were motivated to make best use of the limited photon budget of genetically expressed PA-FPs, they may also be advantageous for 3D PALM-imaging with other photoactivatable and photoswitchable molecules.

Room for improvement remains. First, acquisition speed may be improved with more laser power (for faster bleaching) and brighter dyes or FPs. Given our excitation intensity (~5 kW/cm^2) and exposure time (100 ms), acquiring data for Figures 3–6 took > 10 hours. While data processing speed is comparable to acquisition, parallelization with a GPU-based platform[26] or cluster would improve computational speed. Second, although we reduced background by limiting photoactivation to the focal plane (requiring a 2PA dye), we used widefield excitation. Thus, autofluorescence and spontaneous activation of out-of-focus molecules still impede single-molecule imaging, especially at greater depths. Further improvement is possible if excitation is also confined to the focal plane, perhaps with selective plane illumination[33],[34] or by employing an additional femtosecond laser for excitation as well as activation. Finally, although we consider the generality of our localization algorithm a strength, we suspect accurate models of our PSF and measurement noise would improve localization precision[35].

Methods

Mammalian Expression Vectors

All photoactivatable mCherry fluorescent protein (PA-mCherry1; gift of George Patterson, NIH) expression vectors were constructed using C1 and N1 (Clontech™-style) cloning vectors. In all cases, we started with EGFP (enhanced green fluorescent protein) fusion constructs that have been extensively characterized biochemically and/or cell biologically in the literature. All DNA for transfection was prepared using the Plasmid Maxi kit (QIAGEN, Valencia, CA). To ensure proper localization, PA-mCherry1 fusion proteins were characterized by transfection in HeLa cells (CCL2 line; ATCC, Manassas, VA) using Effectene (QIAGEN) and ~ 1μg vector. Transfected cells were grown on cover glasses in DMEM/F12, fixed after 48 hours, and mounted with Gelvatol for imaging. Epifluorescence images (Supplementary Fig. 16) were captured with a Nikon 80i microscope coupled to a Hamamatsu ORCA-ER camera system using widefield illumination and a Texas Red filter set (Omega; QuantaMax Red), showing proper localizations.

The PA-mCherry1 cDNA was amplified with a 5′ primer encoding an AgeI site and a 3′ primer encoding either a BspEI (C1) or NotI (N1) site for C-terminal and N-terminal fusions (with regards to the FP), respectively. The purified and digested PCR products were ligated into similarly digested EGFP-C1 and EGFP-N1 cloning vector backbones. To generate fusion vectors, the appropriate PA-mCherry1 cloning vector and a targeting cDNA PCR amplification product were digested, either sequentially or doubly, with the appropriate enzymes and ligated together after gel purification. Thus, to prepare PA-mCherry1 N-terminal fusions, the N1 cloning vector was digested with NheI and BamHI and treated with calf intestinal alkaline phosphatase (CIAP). cDNA for the mitochondrial targeting signal (MTS) of human cytochrome C oxidase subunit VIII (cDNA source: Origene; NM_004074.2) was amplified to install NheI and BamHI sites containing a 7-amino acid linker between the targeting DNA sequence and the FP sequence. Likewise, cDNA for human vimentin (cDNA source: Origene; NM_003380.3) was amplified to install NheI and BamHI sites containing a 7-amino acid linker between the targeting DNA sequence and the FP sequence. The amplified PCR products were ligated into the pre-cut PA-mCherry N1 cloning vector to yield MTS-7-PA-mCherry-1 (targeting mitochondria) and vimentin-7-PA-mCherry1 (targeting vimentin in the intermediate filament network). To prepare the PA-mCherry1 fusion to lamin B1, the C1 cloning vector was cut with NheI and BglII and treated with calf intestinal alkaline phosphatase (CIAP). cDNA for human lamin B1 (DNA source: George Patterson; NM_005573.2) was amplified to install NheI and BglII sites containing a 10- amino acid linker between the targeting DNA sequence and the FP sequence. The amplified PCR product was ligated into the pre-cut PA-mCherry C1 cloning vector to yield PA-mCherry-1-10-Lamin B1 (targeting the nuclear envelope). To prepare the PA-mCherry1 endoplasmic reticulum targeting vector, PA-mCherry1-C1 was cut with BspEI and BamHI and treated with calf intestinal alkaline phosphatase (CIAP). A short synthetic oligonucleotide: TCCGGAAAGGACGAGCTGTAAGAATTC containing a 5′ BspEI site and a 3′ BamHI site was then ligated into the cloning vector to establish the KDEL sequence at the C-terminus of PA-mCherry1 with a 2-amino acid linker containing a BspEI site. Next, the N-terminal 51 nucleotides of human calreticulin (cDNA source: Origene;

NM_004343.3) were amplified using primers encoding a 5′NheI site and a 3′ AgeI site and this oligonucleotide was ligated into the similarly cut PA-mCherry1-KDEL vector to produce a derivative containing a 5-amino acid linker between the calreticulin and fluorescent protein sequences and targeting the endoplasmic reticulum. All vector DNA sequences were verified using Big-Dye terminator chemistry on an Applied Biosystems 3130xl Genetic Analyzer with capillary electrophoresis at the Department of Biological Science DNA Sequencing Facility at FSU.

Sample Preparation

Cos7 cells (ATCC) passages 20–30 were grown in T-25 flasks, containing DMEM-HG (Gibco, 31053) supplemented with 10% FBS to 50–70% confluency at 37°C, 5% CO_2. Trypsinized cells were transiently transfected in 35 mm Petri dishes at 4–7*10^5 cells per dish with Fugene 6 transfection reagent (Roche Applied Science, 11814443001), and 0.5 μg plasmid DNA per dish.

Separately, #1.5 mm 25 mm diameter glass coverslips (Warner Instruments, CS-25R15) were cleaned as described previously[23] and coated for ~10 minutes with 10 μg/ml human fibronectin (Millipore, FC010) at room temperature. Transfected cells were then (*i*) transferred to the coverslips; (*ii*) grown as above for 36–48 h; (*iii*) fixed for 15–20 min at room temperature in 4% paraformaldehyde in 1X PBS; and (*iv*) rinsed 3x with PBS, 5% FBS. Vimentin samples also had 0.1% glutaraldehyde added to the fixation buffer. To compensate for sample drift during imaging, prior to data acquisition cells were incubated for 15–30 min with 100 nm Au beads (Microspheres-Nanospheres, 790122-010) diluted ~2x in PBS, before a final rinse with PBS.

Quantum dot samples

Elvax 410 ethylene-vinyl acetate copolymer resin (Dupont) was diluted in toluene to a 4% weight/volume solution by heating overnight at 40°C. The resulting solution was further diluted to 1% by diluting in a 1:1.5:1.5–4% Elvax 410:Quantum Dots (Ocean Nanotech, QSO-520-0010):Toluene ratio. The 1% Elvax/Q dot solution was spin coated (Laurell Technologies Corporation, WS-650S-8NPP-LITE) onto a cleaned 25 mm glass coverslip, by ramping from 0 to 500 rpm over 7 s and maintaining 500 rpm for 40 s. Using atomic force microscopy, we verified that the thickness of the spin-coated film was < 800 nm.

One-photon laser excitation/activation

The home-built one-photon excitation/activation laser illumination system was based on a previously described system[23] (Supplementary Fig. 1). Two lasers were used: a 200 mW, 561 nm laser (561, CrystaLaser, CL561-200) for excitation; and a 100 mW, 405 nm laser (405, Coherent 405–100 CIRCULAR) for activation. Neutral density filters (ND, Edmund Scientific NT54-460) and ½ wave plates (HWP, Thorlabs, AHWP05M-630, WPH05M-405) were used to control the intensity of each beam and custom beam expanders made from lens pairs were used with each laser (561 nm laser: 2.7x BE, Thorlabs f = 15 mm LA1540-A and f = 40 mm LA1304-A; 405 nm laser: 2x BE, Thorlabs f = 15 mm LA1540-A and f = 30 mm LA1289-A) to yield a common beam diameter, thus allowing a common excitation / activation region at the sample.

The 561 nm excitation beam was passed through an acousto-optic tunable filter (AOTF, Quanta Tech, AOTFnC-400.650-TN), used primarily as a fast shutter. The half-wave plates mentioned above (HWP) were used to adjust beam polarization until maximum transmission through the AOTF was achieved. After passing through the AOTF, the 561 nm beam was combined with the 405 nm activation beam using a dichroic beamsplitter (DC, Semrock, FF458-Di02-25×36).

The co-aligned excitation and activation beams were brought to a focus with one lens (FL) and then re-collimated with another (CL). The entire laser illumination system was positioned relative to the imaging microscope such that the front focal plane of lens CL was coincident with the rear focal plane of a 400 mm achromatic relay lens (RL, Edmund, NT49-369-INK) external to the microscope. By doing so, the focus created by lens FL was imaged at the rear pupil of the microscope objective used for excitation, activation and imaging, resulting in widefield illumination. The size of the excitation or activation beam could be controlled by varying the focal length of FL or CL; by choosing FL = 50 mm and CL = 100 mm, a spot of approximately ~35 μm diameter was created at the sample plane.

Two photon activation, standard temporal focus

A temporal focus module based on a previously described system[13] was added to the microscope in order to confine the activation volume (Supplementary Fig. 1). An 80 MHz Ti:Sapphire oscillator capable of producing pulses of 140 fs duration and tuned to 800 nm (800, Coherent, Chameleon Ultra II) was used as the two photon activation source. The 800 nm beam was passed through a Glan-Laser calcite polarizer (POL, Newport, 10GL08AR.16) and a ½ wave plate (HWP, Newport, 10RP52-2), and the wave ½ plate was placed in a motorized rotation mount (Thorlabs, PRM1Z8E) for automated power control. After passing through the polarization optics, the 800 nm beam was passed through a 6.7x beam expander (BE, Thorlabs, f=60 mm AC254-060-B-ML and f=400 mm AC508-400-B-ML NIR coated achromats), and directed at 41.6° onto a 830 grooves/mm gold coated reflective diffraction grating with 21.4° blaze angle (GR, Newport, 53107BK02-035R). The incidence angle of 41.6° was chosen so that the first diffracted order at 800 nm emerged normal to the grating face. The beam was then demagnified 500x to produce a field of view of approximately ~35 μm diameter at the sample plane.

In order to save space on the optical table, the 500x beam demagnification was achieved by placing two expanders in series: an initial de-expansion of 3x (Thorlabs, f=300 mm AC508-300-B-ML and f=100 mm AC254-100-B-ML) and a secondary de-expansion of 167x (Thorlabs, f=500 mm AC508-500-B-ML and Olympus, UPLSAPO60XW f=3 mm objective). The total optical path length required from grating to sample was thus ~2*(300 + 100 + 500 + 3) ~ 1.8 m instead of the ~2*(1500+3) ~3 m required if a single f = 1500 m lens was used to achieve 500x demagnification.

Two photon activation, line scanning temporal focus

For improved confinement of activation, we focused the 2 photon beam onto a line and scanned the line in the direction perpendicular to the grating grooves, in a setup similar to that described previously[22] (Supplementary Fig. 1). A removable mirror mounted on a

magnetic base (RM, Thorlabs, KB1X1) was used to divert the 800 nm beam from the standard temporal focus setup described above, before beam expansion. The resulting beam was redirected to a galvonometric scanner (GAL, Cambridge Technology, 6215HB), aligned so that the scan direction was perpendicular to the grooves on the diffraction grating. The scan mirror was placed ~400 mm from the diffraction grating GR mentioned above, and an f=200 mm cylindrical lens (CFL, Thorlabs, LJ1653L2-B) was used to focus the beam onto GR. Redirection of the scanned beam onto the grating was achieved with another removable mirror RM. A cylindrical beam expander (CBE, Thorlabs, f=30 mm, LJ1212L2-B and f=200 mm, LJ1653L1-B) was placed in the space between galvo and grating, and used to expand the beam 6.7x in the direction perpendicular to the grating grooves. The combination of the 3 cylindrical lenses (beam expander plus focusing lens) produced a line focus that could be scanned perpendicular to the grating grooves, in a manner similar to that previously described[22]. Subsequent 500x demagnification of the line focus was achieved via the beam expanders mentioned above. See Supplementary Note 1 for further rationale of the optical parameters.

Microscope system

PALM imaging was performed on an Olympus IX81 inverted microscope equipped with differential interference contrast (DIC) optics, an additional side port for introduction of an external laser beam (Olympus, IX2-RFACB2-R), and an automated XY stage with an additional Z piezoelectric stage (100 μm range, Applied Scientific Instrumentation, PZ-2000). The aforementioned 400 mm focal length relay lens was used to focus collimated light from the one photon laser illumination system at the rear pupil of a 60x, 1.2NA water immersion objective (Olympus UPLSAPO60XW). This lens provided good transmission of 800 nm activation light while minimizing spherical aberration and focal shifts due to refractive index mismatch that complicate earlier 3D superresolution efforts[16]. An external dichroic mirror (Semrock, Di01-R561-25×36) placed between the relay lens and the laser port combined one photon and two photon illumination sources. Excitation/activation of the sample was achieved via a custom dichroic mirror (Chroma, ZT405/488/561/IR-RPC, reflects 405 nm, 488 nm, 561 nm, 700 nm-1100nm) placed inside a side-mounted Olympus filter cube (Olympus, IX2-MFB-SP-R), and a bandpass emission filter (Semrock, FF01-617/73-25) placed in the same cube served to reject unwanted pump light from the collected fluorescence.

For exciting and imaging PA-mCherry1, the 561 nm laser power was ~85 mW; for one photon activation experiments, the 405 nm laser power rarely exceeded ~ 10 μW; and for two photon activation, we varied average 800 nm laser power from 0 to 600 mW. All powers were measured immediately before the entrance to the objective. Resulting beam profiles for 561 nm excitation and 800 nm scanned temporal focus activation are shown in Supplementary Fig. 3. A 1.6x expander internal to the microscope was engaged for all PALM measurements, and a 1.2x C-mount adaptor (Diagnostic Instruments, DD12BXC) at the microscope output port was used to magnify the final image 60*1.6*1.2 = 115.2x before detection by a back-illuminated, cooled (−65°C), electron-multiplying CCD Camera (EM-CCD, Andor Technology, DU-888E-C00-#BV). The pixel size after magnification was 113 nm. For astigmatic measurements, a 100 mm cylindrical lens (Thorlabs, f=100mm,

LJ1567RM-A) was mounted in a lens tube (Thorlabs, SM1L05) and screwed directly into the female C-mount at the EM-CCD entrance aperture with the appropriate adapter (Thorlabs, SM1A9). The camera+cylindrical lens system was mounted on a rail system (Thorlabs, RLA0600 and RC1) and translated relative to the microscope output port until the imaging plane was displaced ~1 μm from the temporal focus plane, as assayed by monitoring the signal from 100 nm gold fiducial markers.

Distortion correction

Insertion of the cylindrical lens into the emission path introduced a lateral distortion in the images (Supplementary Figure 10). Characterization of the distortion was achieved by imaging gold fiducial markers adhered to a glass coverslip and monitoring the displacement in X and Y as the microscope stage was moved in defined steps. By noting the apparent position of the fiducial markers versus the stage position, effective X and Y pixel sizes were obtained. These pixel sizes (112 nm in X, 147 nm in Y) were constant over the imaging field and for a given position of the cylindrical lens. By plotting the pixels as appropriately-shaped rectangles, the images are corrected for the imaging distortion introduced by the cylindrical lens.

Drift correction

Mechanical and thermal drift during data acquisition was reduced via a commercial focus lock system (Mad City Labs C-Focus System), mounted directly onto the microscope stage and objective as per manufacturer recommendations. We found that the focus lock system reduced axial drift to 200–250 nm over the course of data acquisition. Residual drift is due mostly to thermal or mechanical motion of the coverslip, as the focus lock system is insensitive to motions above the objective. To further correct drift, we monitored the XYZ displacement of 100 nm gold fiducial particles (Microspheres-Nanospheres, 790122-010) via their fluorescence (collected through the same optics used for monitoring PA-mCherry1 fluorescence), nonspecifically adhered to the coverslip as described above. The combination of fiducial tracking with the focus lock system reduced axial drift to < 50 nm.

Data acquisition

We imaged PA-mCherry1 fusions at a frame rate of ~10 Hz, using the highest EM-CCD preamplifier setting of 5x and an EM gain of 300. After finding a transfected cell by exciting the sample at 561 nm, a ‘calibration z stack’ was taken of nearby fiducial markers. If no fiducials were found near a cell of interest, more fiducials were added until at least one was present in the imaging field. A calibration stack consisted of a series of ten images at each z position, with the z piezo moving from −2 μm to + 2μm in steps of 50 nm, and repeated once, for a total of 162 images.

We typically inspected the calibration stack before PALM-imaging cells, because although our 3D localization code works for a range of PSFs, some PSFs are better than others. Strong axial asymmetry of the PSF was often a symptom of spherical aberration, possibly due to variations in coverslip thickness. If the PSF was excessively dim for positive (or negative) defocus, signal-to-noise is worse for defocused molecules in that direction. We reduced excessive axial asymmetry by adjusting the correction collar of our objective.

Strong bilateral asymmetry of the PSF was typically a symptom of excessive coverslip tilt. This asymmetry did not cause obvious problems for our localization algorithm, unless it opposed the astigmatism of the cylindrical lens in our imaging path. Such antagonistic asymmetry typically gave a PSF that varied slowly in the axial direction, reducing axial localization precision. This problem can be mitigated by removing and reinserting the coverslip, taking care to minimize tilt.

After optimizing the PSF, data was acquired at different z piezo positions, separated by 500 nm z steps, often but not always starting at the coverslip surface (for some samples such as PA-mCherry1 lamin constructs, no protein was located at the coverslip surface). We acquired at least 10,000 frames at each z piezo position before advancing 500 nm to the next position, and returned to the same position to acquire more data, until all molecules at a given position were depleted. For z piezo positions other than at the coverslip surface where the fiducial marker was located, we 'jumped' the piezo stage every 200 frames to acquire 20 frames at the z piezo position where the fiducial resided ('fiducial frames'). After each jump, acquisition paused for 30ms to ensure sufficient 'ring down' time of the piezo stage for stabilization at the new z position. Fiducial frames were combined after acquisition for drift correction.

Three dimensional model-independent subdiffractive localization

Following data acquisition, we process the data in the Python programming language[30,36]. Our processing code is open-source and freely available (See Supplementary Software, and http://code.google.com/p/palm3d for the most recent software and documentation). Data processing steps are summarized as follows: (*i*) Construct a calibration stack; (*ii*) Identify candidate particles in each data image; (*iii*) localize each candidate particle using the calibration stack; (*iv*) correct for drift; (*v*) optionally, link localizations and re-localize (*vi*) construct image histograms from localization data. More details are available in Supplementary Note 2. Further discussion of image rendering after localization is discussed in Supplementary Note 3 and Supplementary Table 1.

Supplementary Material

Refer to Web version on PubMed Central for supplementary material.

Acknowledgments

We thank N. Morgan and A. Gillespie for training and use of their spin coater; G. Patterson (National Institute of Biomedical Imaging and Bioengineering) for the gift of purified PA-mCherry1, mEos2 and for the use of his cell culture facilities; A. Jin for measuring the thickness of our quantum dot films; E. Ramko for help with preparing the PA-mCherry1 fusion vectors; K. Kilborn (Intelligent Imaging Innovations) for loaning us the Vector Point Scanning 2P system; and S. Parekh and H. Eden for feedback and suggestions on the manuscript. This work was supported by the Intramural Research Programs of the National Institute of Biomedical Imaging and Bioengineering.

References

1. Larabell CA, Le Gros MA. X-ray Tomography Generates 3-D Reconstructions of the Yeast, *Saccharomyces cerevisiae*, at 60-nm Resolution. Mol Biol Cell. 2004; 15:957–962. [PubMed: 14699066]

2. Hohmann-Marriott MF, et al. Nanoscale 3D cellular imaging by axial scanning transmission electron tomography. Nat Methods. 2009; 6:729–732. [PubMed: 19718033]
3. Gustafsson MGL. Surpassing the lateral resolution limit by a factor of two using structured illumination microscopy. J Microsc. 2000; 198:82–87. [PubMed: 10810003]
4. Gustafsson MGL, et al. Three-Dimensional Resolution Doubling in Wide-Field Fluorescence Microscopy by Structured Illumination. Biophys J. 2008; 94:4957–4970. [PubMed: 18326650]
5. Donnert G, et al. Macromolecular-scale resolution in biological fluorescence microscopy. Proc Natl Acad Sci USA. 2006; 103:11440–11445. [PubMed: 16864773]
6. Schmidt R, et al. Spherical nanosized focal spot unravels the interior of cells. Nat Methods. 2008; 5:539–544. [PubMed: 18488034]
7. Betzig E, et al. Imaging Intracellular Fluorescent Proteins at Nanometer Resolution. Science. 2006; 313:1642–1645. [PubMed: 16902090]
8. Hess ST, Girirajan TPK, Mason MD. Ultra-High Resolution Imaging by Fluorescence Photoactivation Localization Microscopy. Biophys J. 2006; 91:4258–4272. [PubMed: 16980368]
9. Rust MJ, Bates M, Zhuang X. Sub-diffraction-limit imaging by stochastic optical reconstruction microscopy (STORM). Nat Methods. 2006; 3:793–796. [PubMed: 16896339]
10. Huang B, Wang W, Bates M, Zhuang X. Three-Dimensional Super-Resolution Imaging by Stochastic Optical Reconstruction Microscopy. Science. 2008; 319:810–813. [PubMed: 18174397]
11. Shtengel G, et al. Interferometric fluorescent super-resolution microscopy resolves 3D cellular ultrastructure. Proc Natl Acad Sci USA. 2009; 106:3125–3130. [PubMed: 19202073]
12. Axelrod D. Total Internal Reflection Fluorescence Microscopy in Cell Biology. Traffic. 2001; 2:764–774. [PubMed: 11733042]
13. Vaziri A, Tang J, Shroff H, Shank CV. Multilayer three-dimensional super resolution imaging of thick biologicalsamples. Proc Natl Acad Sci USA. 2008; 105:20221–20226. [PubMed: 19088193]
14. Fölling J, et al. Photochromic Rhodamines Provide Nanoscopy with Optical Sectioning. Angew Chem Int Ed Engl. 2007; 46:6266–6270. [PubMed: 17640007]
15. Mlodzianoski MJ, Juette MF, Beane GL, Bewersdorf J. Experimental characterization of 3D localization techniques for particle-tracking and super-resolution microscopy. Opt Express. 2009; 17:8264–8277. [PubMed: 19434159]
16. Huang B, Jones SA, Brandenburg B, Zhuang X. Whole-cell 3D STORM reveals interactions between cellular structures with nanometer-scale resolution. Nat Methods. 2008; 5:1047–1052. [PubMed: 19029906]
17. Subach FV, et al. Photoactivatable mCherry for high-resolution two-color fluorescence microscopy. Nat Methods. 2009; 6:153–159. [PubMed: 19169259]
18. Denk W, Strickler JH, Webb WW. Two-Photon Laser Scanning Fluorescence Microscopy. Science. 1990; 248:73–76. [PubMed: 2321027]
19. Zhu G, van Howe J, Durst M, Zipfel W, Xu C. Simultaneous spatial and temporal focusing of femtosecond pulses. Opt Express. 2005; 13:2153–2159. [PubMed: 19495103]
20. Oron D, Tal E, Silberberg Y. Scanningless depth-resolved microscopy. Opt Express. 2005; 13:1468–1476. [PubMed: 19495022]
21. Ando R, Mizuno H, Miyawaki A. Regulated Fast Nucleocytoplasmic Shuttling Observed by Reversible Protein Highlighting. Science. 2004; 306:1370–1373. [PubMed: 15550670]
22. Tal E, Oron D, Silberberg Y. Improved depth resolution in video-rate line-scanning multiphoton microscopy using temporal focusing. Opt Lett. 2005; 30:1686–1688. [PubMed: 16075538]
23. Shroff H, et al. Dual-color superresolution imaging of genetically expressed probes within individual adhesion complexes. Proc Natl Acad Sci USA. 2007; 104:20308–20313. [PubMed: 18077327]
24. Juette MF, et al. Three-dimensional sub-100 nm resolution fluorescence microscopy of thick samples. Nat Methods. 2008; 5:527–529. [PubMed: 18469823]
25. Pavani SRP, et al. Three-dimensional, single-molecule fluorescence imaging beyond the diffraction limit by using a double-helix point spread function. Proc Natl Acad Sci USA. 2009; 106:2995–2999. [PubMed: 19211795]

26. Smith CS, Joseph N, Rieger B, Lidke KA. Fast, single-molecule localization that achieves theoretically minimum uncertainty. Nat Methods. 2010; 7:373–375. [PubMed: 20364146]
27. Pertsinidis A, Zhang Y, Chu S. Subnanometre single-molecule localization, registration, and distance measurements. Nature. 2010; 466:647–651. [PubMed: 20613725]
28. Arimoto R, Murray JM. A common aberration with water-immersion objective lenses. J Microsc. 2004; 216:49–51. [PubMed: 15369482]
29. Guizar-Sicairos M, Thurman ST, Fienup JR. Efficient subpixel image registration algorithms. Opt Lett. 2008; 33:156–158. [PubMed: 18197224]
30. Oliphant T. Python for Scientific Computing. Comput Sci Eng. 2007; 9:10–20.
31. Gupton SL, Collings DA, Allen NS. Endoplasmic reticulum targeted GFP reveals ER organization in tobacco NT-1 cells during cell division. Plant Physiol Biochem. 2006; 44:95–105. [PubMed: 16647266]
32. Yoon M, Moir RD, Prahlad V, Goldman RD. Motile Properties of Vimentin Intermediate Filament Networks in Living Cells. J Cell Biol. 1998; 143:147–157. [PubMed: 9763427]
33. Huisken J, Swoger J, Del Bene F, Wittbrodt J, Stelzer EHK. Optical Sectioning Deep Inside Live Embryos by Selective Plane Illumination Microscopy. Science. 2004; 305:1007–1009. [PubMed: 15310904]
34. Ritter JG, Veith R, Jan-Peter S, Kubitscheck U. High-contrast single-particle tracking by selective focal plane illumination microscopy. Opt Express. 2008; 16:7142–7152. [PubMed: 18545417]
35. Mortensen KI, Churchman LS, Spudich JA, Flyvbjerg H. Optimized localization analysis for single-molecule tracking and super-resolution microscopy. Nat Methods. 2010; 7:377–381. [PubMed: 20364147]
36. Hunter JD. Matplotlib: A 2D Graphics Environment. Comput Sci Eng. 2007; 9:90–95.

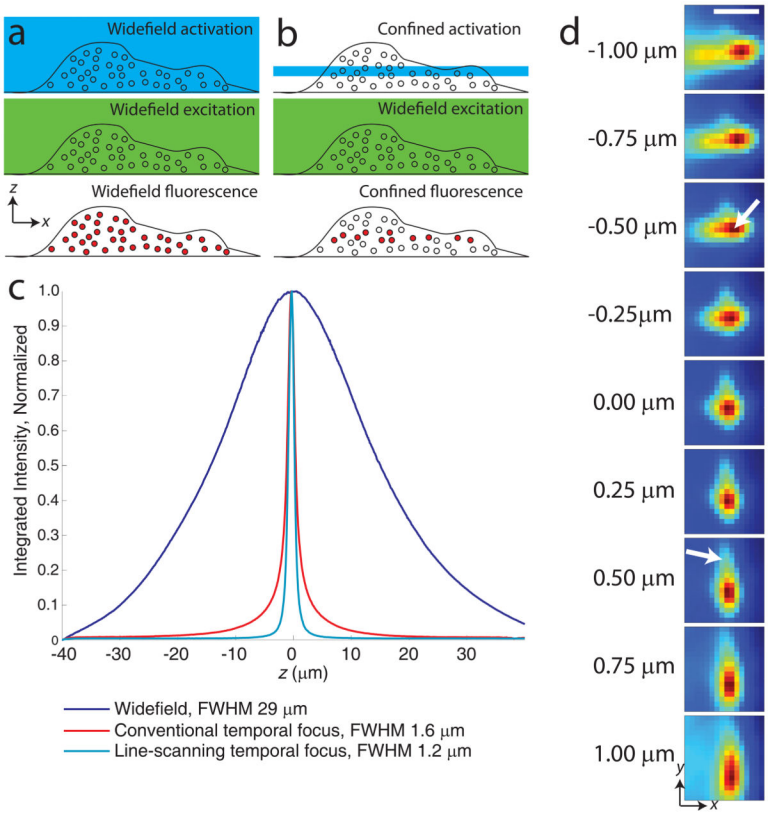

Figure 1.

Experimental considerations for 3D PALM. **(a)** Widefield activation (top panel) and excitation (middle panel) for localizing molecules (circles) throughout the entire cellular volume (bottom panel, filled circles). **(b)** Confined activation with widefield excitation for localization. **(c)** Sectioning performance of different illumination modalities. Integrated axial response of ~800 nm thick quantum dot film, moved through 80 μm axial range in 100 nm steps.Fluorescence was integrated over a 25 μm by 25 μm area, yielding the axial response under widefield (488 nm, blue), conventional- (800 nm, red), and line-scanning- temporal focus (800 nm, cyan) illumination. The latter shows reduced full width at half maximum (FWHM) compared to other excitation configurations, and reduced 'tails' at z positions further from focus. **(d)** Images of a 100 nm gold bead at different axial positions. The PSF shape is only coarsely approximated by an elliptical Gaussian function, as aberrations cause the intensity center-of-mass of the PSF to vary axially and 'tails' to vary asymmetrically (arrows). Scale bar 1 μm.

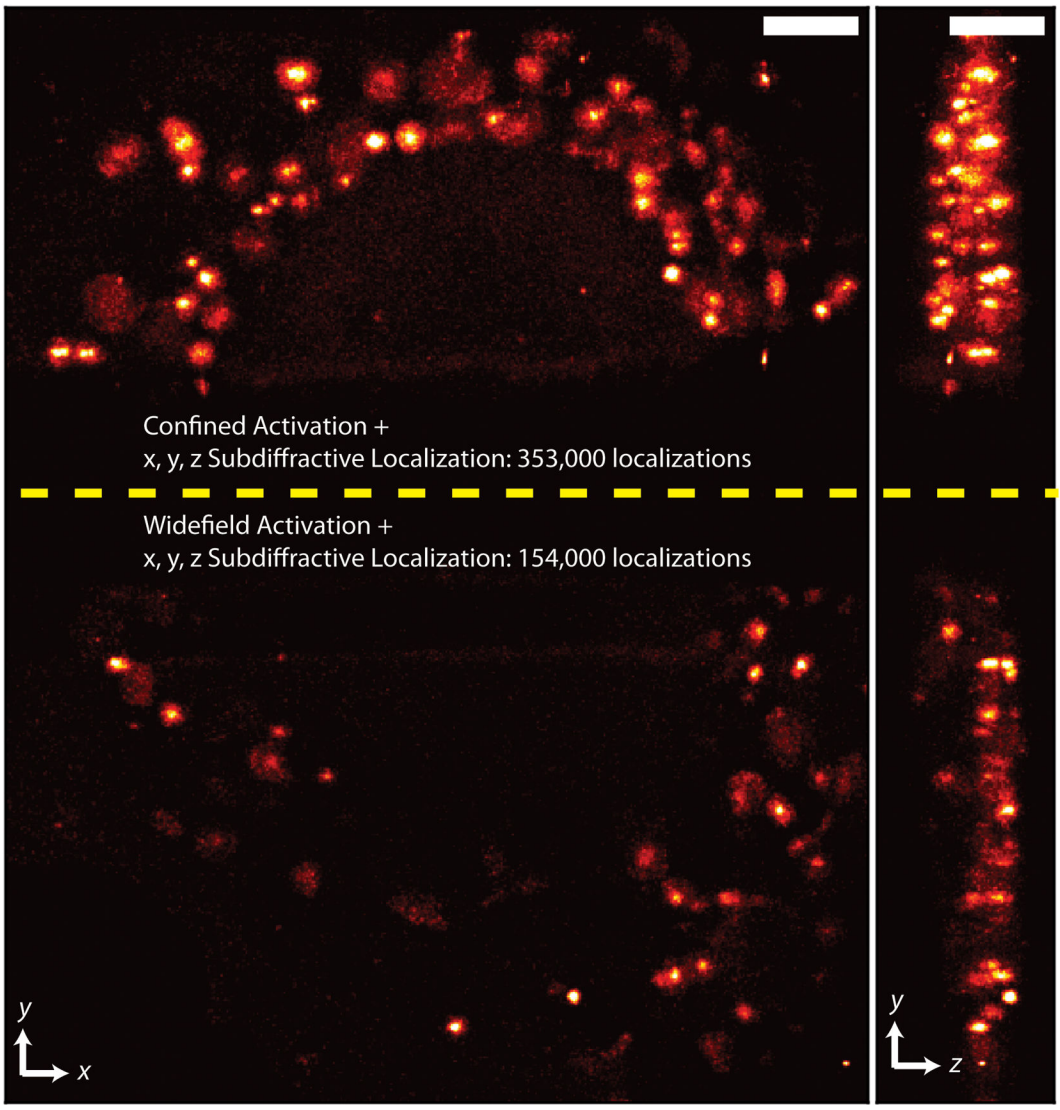

Figure 2.

Improvement over existing 3D PALM. A Cos7 cell expressing PA-mCherry1 targeted to the mitochondrial matrix was simultaneously PALM- imaged with both confined (above dashed yellow line) and widefield (below dashed line) activation. Left: xy maximum-intensity projection. Right: zy maximum-intensity projection. The colormap is identical over the entire image. Scale bars 3 μm.

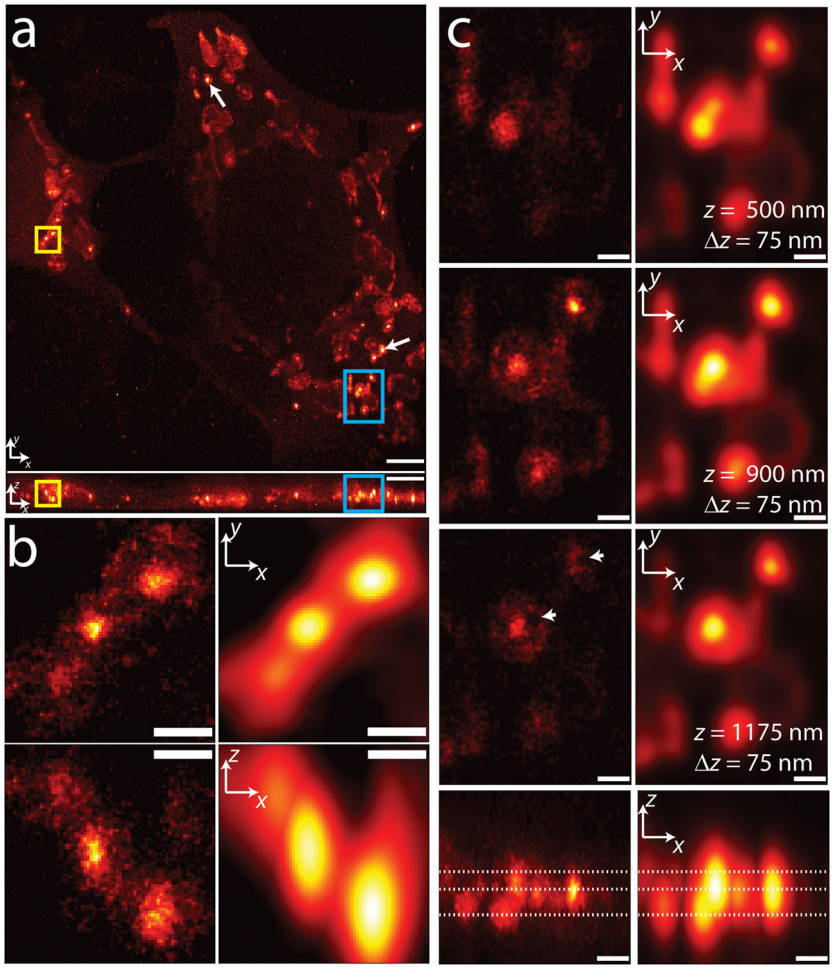

Figure 3.

3D superresolution imaging of a mitochondrial network. **(a)** xy (top) and xz (bottom) maximum intensity projections of mitochondrial matrix labeled with PA-mCherry1. White arrows show examples of 'core' regions of higher intensity inside mitochondria. ~1.2 million unlinked localizations are rendered in each view. **(b)** Higher magnification xy (top) and xz (bottom) views of the yellow rectangular regions in **(a)**, with both super-resolved (left) and diffraction-limited (right) views compared. **(c)** Higher magnification xy sections (top three rows) and xz maximum intensity projections (bottom row) of the blue rectangular regions highlighted in **(a)**. xy sections are constructed from all localizations in a 75 nm thick z region, and relative z locations are indicated by dotted lines shown in the xz maximum intensity projection. Both superresolved (left) and diffraction-limited (right) views are shown. Arrowheads indicate void regions that are invisible in the diffraction limited views. Only localizations with correlation strength >0.4 are shown. Histogram bin sizes are 60 nm for **(a)** and 25 nm for **(b)** and **(c)**. Supplementary Video 1 steps through xy slices with 60 nm pixel size and 60 nm z separation. Scale bars, 3 μm (**a**); 0.5 μm (**b**); 0.5 μm (**c**).

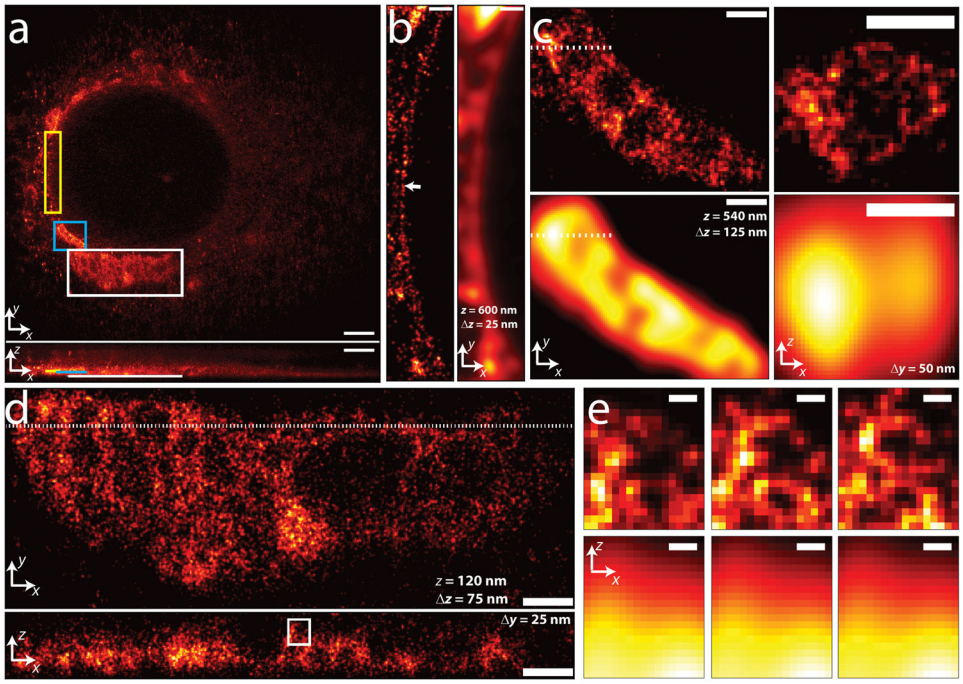

Figure 4.

3D superresolution imaging of an ER network. **(a)** xy (top) and xz (bottom) maximum intensity projections of PA-mCherry1 targeted to the endoplasmic reticulum. ~820,000 unlinked localizations are rendered. **(b)** Magnified xy views of yellow rectangular region in **(a)**, comparing super-resolved (left) and diffraction-limited (right) views. Localizations within a 25 nm z slice centered 600 nm above the coverslip are shown. Arrow highlights nuclear membrane, resolved to ~25 nm. **(c)** Magnification of blue rectangular region in **(a)**. Superresolved xy (left, 125 nm z slice centered 540 nm above coverslip) and xz (right, corresponding to the dotted line in xy view, 50 nm y slice) views are shown in top row, corresponding diffraction-limited images in bottom row. **(d)** Magnification of white rectangular region in **(a)**. Superresolved xy (top, 75 nm z slice centered 120 nm above coverslip) and xz (bottom, corresponding to the dotted line in xy view, 25 nm y slice) views are shown. **(e)** Magnification of white rectangular region in **(d)**, showing superresolved (top row) and diffraction-limited (bottom row) xz views. Three successive xz views, 25 nm thick in y, 25 nm y spacing between each view are shown. Localizations with correlation strength >0.4 are shown. Histogram bin sizes: 60 nm for **(a),** 25 nm for **(b)–(e)**. Supplementary Video 2 steps through xy slices with 60 nm pixel size and 60 nm z separation. Scale bars, 3 μm (**a**); 0.5 μm (**b**); 0.5 μm (**c**); 0.5 μm (**d**); 0.1 μm (**e**).

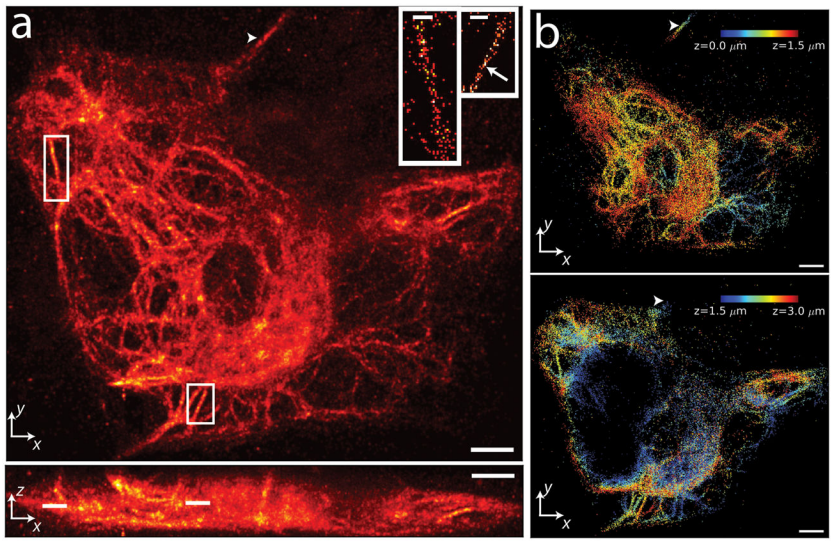

Figure 5.

3D PALM-imaging of a vimentin network. **(a)** xy (top) and xz (bottom) maximum intensity projections of PA-mCherry1-vimentin. ~1 million unlinked localizations are rendered in each view. Insets show further magnification of white rectangles in xy (lines in xz) maximum intensity projection, highlighting individual vimentin fibrils in 60nm thick z slices (localizations are linked). Scale bar in each inset, 600 nm. Arrow indicates a region of fibril with apparent width < 100 nm. **(b)** Axial extent of vimentin network with z location indicated as a colormap. For clarity, localizations corresponding to 0–1.5 μm (top panel) and from 1.5–3 μm (bottom panel) are shown separately. Arrowheads in **(a), (b)** indicate a fibril that persists over > 2μm axially. Only linked localizations with correlation strength >0.4 are shown. Histogram bin sizes are 60 nm for all subfigures. Supplementary Video 3 steps through xy slices with 60 nm pixel size and 60 nm z separation. Scale bars 3 μm (**a**); 3 μm (**b**).

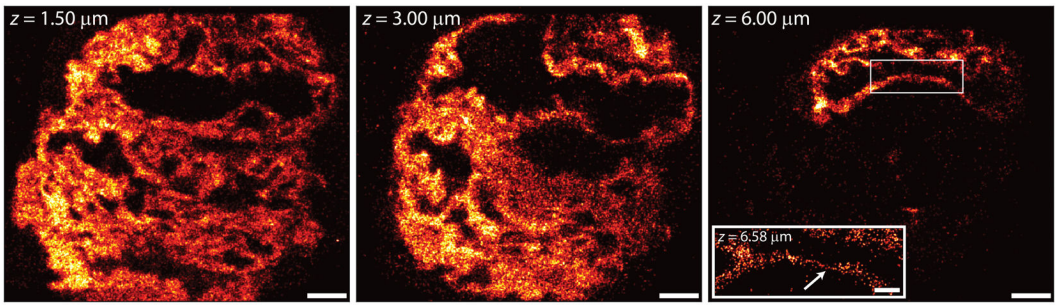

Figure 6.

3D PALM image up to ~7.5 microns in depth. 50 nm-thick xy slices of PA-mCherry1-lamin B1 fusions in a fixed Cos7 cell, at axial depths of 1.5- (left), 3- (middle), and 6 µm (right); scale bars 3 µm. A magnified view (inset) of the highlighted region shows a thin section of membrane resolved to ~50 nm at an axial depth of 6.58 µm (indicated by arrow); scale bar 1 µm. Only localizations with a correlation strength >0.4 are shown, bin sizes are 50 nm (main panels) and 25 nm (inset). Supplementary Video 4 steps through xy slices of this 3D image with 50 nm pixel size and 50 nm z separation, rendered from ~1.9 million unlinked localizations.